

CFD ANALYSIS OF THE CIAM/NASA SCRAMJET

C.G. Rodriguez*
Allied Aerospace, GASL Div.,
Hampton, VA 23681-0001.

Abstract

The CIAM/NASA flight test was numerically analyzed. The flowpath was divided into inlet and burner sections, and solved sequentially. Initial simulation of the inlet at high-speed conditions failed to describe the behavior of the data, which indicated the existence of separation. An analysis of low-speed operation showed inlet unstart and subsequent hysteresis effects which qualitatively approximates the data. Simulation of the burner predicts dual-mode operation, as the data suggests, although peak pressures were somewhat underpredicted. Effects of grid convergence, turbulent Schmidt number and chemistry models were evaluated. It is concluded that current CFD tools may be used to anticipate effects of design and construction in actual operations.

Nomenclature

k	turbulence kinetic energy [m^2/s^2]
M	Mach number
P	static pressure [Pa]
Sc_T	turbulent Schmidt number
t	time [s]
T	static temperature [K]
T_0	total temperature [K]
U	velocity [m/s]
w	mass flowrate [kg/s]
x	axial (streamwise) coordinate [m]
y	vertical coordinate [m]
y_i	mass-fraction of specie i
z	lateral coordinate [m]
y^+	dimensionless vertical turbulence coordinate
ρ	density [kg/m^3]
η_c	combustion efficiency
η_{mix}	mixing efficiency
τ	turbulence intensity
ω	specific dissipation rate [1/s]
μ_T/μ_L	turbulent/laminar viscosity ratio

1. Introduction

Under contract from NASA, Russia's Central Institute of Aviation Motors (CIAM) designed and built an axisymmetric, dual-mode scramjet engine. On February 12, 1998 this engine flew on the nose of a modified SA-5 missile. It was fueled with hydrogen for about 77 seconds, and achieved the longest duration, dual-mode, scramjet-powered flight-test up to date^{1,2}.

1.1. Description of the experiment

The design layout of the engine is shown in figure 1. It includes:

- an external/internal, axisymmetric, Mach-6 inlet,
- a burner section with three fuel-injection stages,

* Senior Engineer, Member AIAA

- an expansion section with a partial nozzle. Except for the external inlet, most of the engine consists of an annular duct between the body of the engine and an external cowl. This cowl is held in place by two sets of struts.

The external inlet begins at the nose-tip which incorporates a pitot probe. The body itself consists of three conical segments with increasing half-angles. The internal inlet starts at the location of the blunt cowl-lip. Body-side expansions and cowl-side compressions are used to turn the flow parallel to the body center-line by the time it reaches a diverging isolator, upstream of the first row of injectors.

The burner consists of three injector stages, denoted I, II, and III in figure 1,c). Each stage has 42 injectors; the injectors of stages I and II are aligned, and interdigitated with those of stage III. Stages I and II are located near each of the two body-side cavities, while stage III is located at the cowl step. Hydrogen fuel was intended to be injected through all three stages. Stages II and III were to operate during most of the flight regime; stage I was supposed to operate above Mach 5, when supersonic combustion was expected.

As mentioned before, two sets of struts hold the engine together; each set consists of four struts. The first set is placed at the internal inlet; these struts have a small cross-section, and presumably have very little impact on the flow in the region. The second set is located towards the end of the engine, near the exit-nozzle throat; these struts have a large cross-section. At this axial location, the cowl expands to compensate for the resulting area blockage. The cowl ends by opening up into an exit nozzle.

During manufacture of the engine, the internal flowpath was altered due to structural reinforcements, weld beads and surface deformation resulting from the welding. There is still considerable uncertainty regarding the final configuration. To add to this geometry uncertainty, post-test inspection of the engine showed combustor-liner deformations²; these deformations have not been quantified. In any case, the (presumed) as-built pre-test flowpath was used for the present calculations.

A brief description of the flight test follows. While the booster was still burning, fuel addition took place within the scramjet (approximately 38 s into the flight) at a flight Mach number of 3.5. The maximum-velocity condition occurred at booster burnout, at a Mach of 6.4 (around 56 s). After burnout, the scramjet/missile combination followed a ballistic trajectory, with increasing altitude (and decreasing dynamic pressure) until a maximum altitude was reached (90 s). Afterwards, dynamic pressure increased until flight termination (115 s). Fuel addition continued all the way to termina-

tion, except for a brief period around 90 s.

Several anomalies and deviations from planned flight-test conditions occurred. First, the test took place at an altitude lower than anticipated. In particular, the maximum-velocity condition occurred at 21.6 km rather than 24 km; the resulting dynamic pressure and mass inflow were double the design values. Furthermore, an apparent failure in the fuel control-system resulted in excessive fuel flowrate and engine unstart for about 12 s. The control system responded by drastically reducing the fuel flowrates of stages II and III. This allowed the engine to restart at about 50 s (Mach 5.0). However, the possible presence of large flow-separation near the inlet throat caused the controls to keep stage I shut. As a result, combustion took place with only stages II and III active.

1.2. Previous Work and Present Approach

Previous to the present work, an analysis of the operation of the inlet design at planned test conditions was done by Hawkins³. It predicted inlet start at the planned operating conditions; it also found the presence of small separation bubbles just behind the cowl lip and in the body side, mainly because of shock impingement. Gaffney and Sanetrik⁴ performed a CFD analysis of the full engine using the VULCAN code. The design geometry and planned free-stream conditions at the maximum-velocity point were used; the total fuel flow-rate was similar to the experiment. To reduce computational expense, the entire flow was assumed axisymmetric; the rings of injector holes were replaced by axisymmetric slots of equivalent total area. Their calculated Mach contours within the burner suggests that the average Mach was subsonic, or nearly so.

The present work documents an ongoing investigation of the CIAM flight test as it actually occurred, based on the best available information; some early results were reported elsewhere⁵⁻⁶. As mentioned before, the as-built geometry will be modeled; no attempt was made to account for possible in-flight deformation. The operating conditions chosen for analysis correspond to the maximum-velocity point in the flight-test trajectory. As explained before, only stages II and III actually worked at the chosen operating condition. Therefore, for the purposes of this paper, “inlet” will denote the domain from a point upstream of the nose, to a section in the duct just upstream of stage II; the remaining duct will be considered the “burner”. Note that, with these definitions, the inlet throat will be the minimum area just ahead of stage I injectors. The inlet and burner were solved separate and sequentially.

The VULCAN code was chosen for the present investigation. VULCAN is a general purpose CFD code that can solve the Reynolds-averaged Navier-Stokes equations. It has a wide array of physical, turbulence and chemistry models available. A full description may be found in the literature ⁷. The specifics of its application to the present work will be described throughout the paper.

2. Inlet

2.1. Solution Procedure

Since the inlet geometry (not accounting for stage I injectors) is axisymmetric, the axisymmetric form of the governing equations was solved with VULCAN for the obvious computational benefits. The actual grid was two-dimensional, with approximately 192,000 control volumes (CV) divided among 15 blocks to facilitate the use of VULCAN's MPI capabilities; 100 CVs were used along the duct height. The block configuration can be seen in figure 2,a), with a detail of the grid in the neighborhood of the throat also shown (b). The maximum wall spacing was less than 0.03 mm; the maximum y^+ was below 30, and occurred near the throat. The grid was mostly C(0)-continuous, except in the neighborhood of the cowl lip.

All inflow boundaries were set at free-stream conditions, while extrapolation was used for outflow boundaries. Initially, the free-stream conditions were set to correspond to the maximum-velocity point in the trajectory (56.5 s into the flight) (see table 1 - the values for the turbulent intensity τ and viscosity-ratio μ_T/μ_L were assumed); other free-stream conditions were used for reasons that will become clear later in this paper. All walls were modeled as no-slip with prescribed temperatures. The wall temperatures were taken from the measured values. For convenience, these were assumed to be stepwise-constant along segments of the walls. No attempt was made to exactly match the temperature value at the probe locations; instead, the smoothest possible distribution was imposed.

T [K]	203.5
p [Pa]	3968
M	6.4
τ	.01
μ_T/μ_L	1.0

Table 1: Free-stream conditions at $t = 56$ s.

The gas was assumed to be a single-specie, thermally-perfect air. To model the inviscid fluxes, Edwards' low-dissipation flux-split scheme was used, together with third-order MUSCL extrapolation and Van Leer's limiter. Wilcox' 1998 $k-\omega$ model⁸ was used for turbulence modeling, coupled with Wilcox's wall-matching functions at the solid walls. The turbulent Prandtl number was set at 0.90. Transition from laminar to turbulent was imposed at the first change in slope in the external inlet. This location is close to the one predicted by the usual conical-flow transition-criteria³ ($Re_\theta/M_e = 150$). In VULCAN, transition can be approximated by using "laminar regions", or regions where source terms in the turbulence equations are turned off. Time-integration was performed with the implicit diagonalized approximate-factorization (DAF) scheme. For most of the calculations, the local CFL number was set at 2.0. The entire flowfield was solved elliptically, in spite of being mostly supersonic, in an attempt to capture all the possible separation regions present in the domain. As may be recalled from the previous discussion, data suggest the presence of large separation at the beginning of the internal inlet; smaller separation bubbles may also be expected at shock-impingement locations. To reduce computational times, VULCAN's MPI capability was used. The calculations were done on an Origin 2000 using 12 R10000 250 MHz processors; the resulting parallel ideal speed-up was 11.40. Wall-time CPU was approximately 0.165 ms per CV per iteration. Determination of convergence by residual drop was not possible because of large oscillations in the residual. Most of these oscillations appear to occur in the first two blocks, around the pitot nose. Attempts to eliminate or reduce these oscillations were unsuccessful. Therefore, convergence was assumed when no change could be observed in the overall domain and wall-pressure trace. To accelerate convergence, grid sequencing was adopted with three sequences: coarse, medium, and fine. About 25,000 iterations were required (including about 7,500 for the fine sequence). This procedure was also used to give some measure of grid convergence, as will be shown in the results section.

2.1 Results

The Mach contours for the complete inlet solution may be seen in figure 3, a) and b). A conical bow-shock forms at the nose of the spike, detached from the body. Additional shock-waves are formed at the compression corners of the external inlet. All these shocks coalesce and end at the cowl lip (where another bow shock is originated). This flow configuration agrees with previous solutions^{3, 4}. A closer look at the internal inlet flowfield [figure 3, b)] shows the presence of small recirculation bubbles, particularly at the cowl lip and at the structural

reinforcement. However, there is no evidence of the massive separation suggested by the data. The lack of separation is apparent in the wall-pressure trace (figure 4-a), where the numerical distribution is compared with the data. The numerical results show a dip in the pressure trace in coincidence with the first body-side expansion (at about 440 mm). The data, on the other hand, show continuously-increasing pressure at that point which is consistent with boundary-layer separation. Overall, the calculated pressures agree well with the data up to the point of the possible separation. Downstream from there, the predicted pressure levels are considerably lower than what the data suggest. The calculated mass-average Mach number at the exit is approximately 2.67, which is much higher than the value of 2.0 predicted by a one-dimensional analysis of the data². The comparison of the body wall pressures for the medium and fine grid sequences is presented in 4,b); the two solutions are sufficiently close for the fine sequence to be considered acceptable. Clearly, a straightforward approach fails to capture the behavior shown by the data.

Voland et al² suggested that the inlet separation may have been caused by changes in the inlet geometry (with respect to the design) or by a hysteresis in the inlet starting process (or a combination of both); in the latter case, the massive separation created during the inlet unstart may have survived after the restart. Previous numerical experimentation performed by the author⁵ showed that, after an artificially-induced inlet unstart, a separation region would remain in place near the throat even after removal of the cause. Furthermore, analysis of the flight data indicates that the inlet was unstarted before and up to the time fuel flowrate was turned on⁶. If all this is true, then a massive separation may have been created during low-speed operation (leading to inlet unstart), and because of hysteresis some of it remained in place even after reaching design flight conditions (and after the inlet restarted).

In order to have at least a qualitative insight into the phenomena, three points in the trajectory were run sequentially (see table 2); $t = 38$ s corresponds to the point immediately before fuel addition. The first two conditions were run fully-turbulent, and with constant wall temperatures (at an average of the experimental data); the $t = 56$ s condition was run exactly as described before (but obviously with different initial conditions). Each condition was run for 15,000 iterations and with the same convergence criteria as before.

t [s]	25	38	56
T [K]	211	212	203.5
p [Pa]	21710	9740	3960
M	2.57	3.51	6.4

Table 2: Free-stream conditions at several points in the flight trajectory.

The results are shown in figures 5 to 7. At $t = 25$ s (figure 5) the shocks coming from the external inlet (not shown here) are far ahead of the inlet and do not interfere with the cowl lip. As a result, the shock coming from the lip is unobstructed and impinges on the body side, resulting in the separation of the boundary layer (this process likely started earlier in the trajectory). The recirculation region creates a shock that ends up ahead of the inlet. Therefore, the numerical simulation indicates that the inlet was unstarted under these flow conditions. The fair qualitative agreement with the data suggests that this may also have been the case during the flight. By $t = 38$ s (figure 6) the inlet is still unstarted, as both data and CFD show. It should be noted that, under these conditions, the numerical flow appeared to be highly transient, with the body-wall recirculation increasing and decreasing in size; shown in the figure is the recirculation at its smallest. Finally, at the maximum-velocity point of $t = 56$ s (figure 7) the inlet has restarted, but a recirculation region remains at the throat; this seems to be consistent with the data. There was a small unsteadiness associated with the recirculation shape, but without any major change in size. There is a better qualitative agreement with the pressure data, compared with the straightforward approach at the same conditions (see figure 4), but the pressure levels are still low; the mass-averaged exit Mach number is about 2.40.

Earlier attempts⁶ to model the conditions between 38 s and 56 s failed to predict restart at 50 s (the inlet still restarted at 56 s); upstream interaction from dual-mode combustion may have played a part. In any case, it is acknowledged that the procedure outlined above is, at best, a qualitative approximation to the full simulation of the flight trajectory. This would require a time-accurate simulation of the full engine, with all three injector stages in operation. The theory presented above was meant to provide a plausible explanation of the behavior shown by the data, which could not be reproduced by a more direct approach.

3. Burner

3.1 Solution Procedure

Burner calculations were done on a three-dimensional slice limited by the jet-centerplanes between adjacent stage II and III injectors; this domain corresponds to about 4.3 degrees of the annular combustor (see figure 1, b). To simplify the grid generation, and since the resulting width was much smaller than the body radius, the domain was approximated as rectangular and with the jet centerplanes parallel to each other and normal to the body and cowl walls.

The grid was discretized into approximately 2.8 million CVs, distributed among 48 blocks (figure 8). The number of CVs ranged from 76 to 132 in the vertical direction, and from 28 to 36 laterally; the higher numbers correspond to the vicinity of the injectors. The wall spacing varied from 0.1 mm at the inlet to 0.5 mm towards the exit. The resulting y^+ was mostly under 100, except near the exit nozzle where the flow accelerated to supersonic conditions (as will be shown later), and where the y^+ could be as high as 200. Non-C(0) grid blocks were used throughout the geometry, especially near the injectors, to reduce computational effort. It should be noted that the area increase immediately before the exit nozzle in the experimental configuration is missing from the computational domain; as mentioned before, this expansion was meant to compensate for the rear-struts blockage. Since these struts are not being modeled, the area was held constant in the numerical simulation.

Unless otherwise noted, all calculations were done with the conditions and procedure to be described next (hereafter known as baseline conditions). At the jet-centerplanes, symmetry boundary conditions were imposed. No-slip, prescribed temperature conditions were used at the walls, with the experimentally-measured temperatures approximated in the same way as in the inlet. An extrapolation boundary condition was used at the exit. Hydrogen fuel was injected at sonic conditions through stages II and III, and at the angles shown in figure 1,c). The resulting mass flowrates gave an overall equivalence ratio of about 0.60. At the location of the injectors, fixed boundary conditions were imposed using the values of table 3.

	Stage II	Stage III
M	1.0	1.0
T_0 [K]	716	771
T [K]	597	642
U [m/s]	1864	1934
ρ [kg/m ³]	0.155	0.149
w [kg/s]	0.042	0.042

Table 3: Injectant conditions.

As for the inlet conditions, the results from the inlet calculations were not deemed accurate enough to be used as inflow conditions for the burner calculation. Therefore, a uniform-inlet condition was used, such that it gave the same mass-flowrate, mass-averaged total-temperature and turbulence conditions as the inlet exit conditions for $t = 56s$ (with inlet separation), and with a Mach number of 2.0. These conditions are summarized in table 4.

T_0 [K]	1632
ρ [kg/s]	0.467
M	2.0
τ	.06
μ_T/μ_L	350

Table 4: Inlet conditions for burner calculations.

The solution procedure was similar to the one employed for the inlet simulation; only those features that were different will be detailed in this section. The gas was assumed to be a mixture of thermally-perfect gases. The chemistry model used was NASA Langley's 7-specie/7-reaction (7x7) model⁹. At the operating conditions, this model was difficult to autoignite⁴; therefore, both a 1-step reaction model and VULCAN's ignition regions were alternatively used with success to initiate the reaction. The turbulent Prandtl and Schmidt numbers were set at 1.0. Turbulence modeling also used Wilcox's compressibility correction⁸ to model Mach number effects on mixing. As before, a three-grid sequence was used for convergence acceleration. Maximum CFL used was 5.0. Approximately 60,000 iterations were used, of which about 40,000 corre-

sponded to the fine sequence; convergence will be discussed in the next subsection. 48 R10000 400 MHz processors were used, with a resulting ideal speed-up of 47.0. Wall-time CPU was approximately 0.264 ms per CV per iteration.

3.2 Results

Figures 9 and 10 show the Mach and water mass-fraction contours, respectively, for the vertical plane midway between the two injectors. A low-speed flow region begins at the step on the cowl wall, and extends just past the cavity. The core flow is supersonic up to $x \sim 950$ mm, where it begins to decelerate through a shock train to almost sonic conditions; this is confirmed by the mass-averaged one-dimensional Mach distribution (figure 12). The flow finally reaccelerates to supersonic conditions at the nozzle exit. The extent of the reaction may be judged from the water contours and the axial distribution of efficiencies^a (figure 11). Most of the fuel from stage II appears to have mixed by the time it reaches the stage III axial-location. Due to ignition delay, however, it starts to react shortly before that location, and appears consumed by the time it reaches the constant-area section ($x \sim 900$ mm). Stage III fuel, on the other hand, seems to start reacting in the constant section, contributing perhaps to the choking of the flow. All the fuel is mixed, and almost all (94%) reacted, by the time it reaches the exit.

Comparing the calculated wall pressure-traces with the data (figure 13), CFD somewhat underpredicts the pressures up to $x \sim 900$. Furthermore, it shows a reacceleration or supersonic region just downstream of the cavity, corresponding to the closing of the cowl-wall low-speed region (this can also be seen in the one-dimensional average of figure 12); the data does not show reacceleration at that location. Downstream from there, the numerical pressures recover their values before reacceleration, and remain fairly constant (in coincidence with the subsonic region) until reaching the exit nozzle; the experimental pressures also appear constant but at a somewhat higher value. There was some unsteadiness in the fine-sequence solution between 800 and 900 mm, approximately; a fully steady-state solution was not achieved. The origin of this unsteadiness was most likely the recirculation region, and it resulted in changes in the pressure levels of about 10 Kpa in this region; these values alternated for the last 25,000 iterations, and the results shown correspond to the lowest pressures.

The effects of grid sequencing (and therefore grid convergence) are shown in figure 14 for the body wall-pressures.

a. η_{mix} and η_{c} are defined¹⁰ as mixed fuel over total fuel, and reacted (water) fuel over total fuel, respectively (all evaluated at local axial planes).

There are small differences at the inlet and toward the exit; the maximum burner pressure seem to be the same for both grids. Taking into account that these differences correspond to a factor of 8 in the number of CVs, it can be argued that the solution is at least close to being grid-converged. Since the medium sequence appears to give a qualitatively good solution it was used to perform a series of parametric studies. In what follows, all results correspond to the medium sequence unless otherwise noted.

Lowering the turbulent Schmidt number (Sc_T) from 1.0 to 0.5 (figure 15) and turning the compressibility correction off enhances the mixing and heat release and increases the pressure in the near-field ($x < 800$ mm). However, it gives a much larger supersonic region and lower pressure after choking. It would seem that too much heat release immediately after stage III reduces the pressure levels in the constant-area section. Apparently, most of the heat-release should occur between injector stages and downstream of the cavity to have maximum effect on the pressure rise; it is not immediately obvious how to achieve this with a constant-Sc model. Strong sensitivity of dual-mode combustion to turbulent transport coefficients has been reported in the literature¹¹.

Switching from a 7x7 to a 9x18 chemistry model⁹ (all other conditions left at their baseline values) does not appear to have a major impact on the solution (figure 16); the efficiency distributions (not shown here) are somewhat lower in the near field, but otherwise very close to the 7x7 model. Since more ignition delay was expected from the 9x18 model, this issue may require further investigation.

4. Summary

The CIAM/NASA scramjet flight-test was subjected to a CFD analysis. The data from the experiment shows that the inlet was unstarted from a free-stream Mach number of about 2.5 to about 5.0 (including the start of fuel injection); even after restart, separated flow remained just ahead of the throat up to the Mach 6.4 condition being evaluated in the present paper.

CFD analysis performed at the Mach 6.4 condition suggests that the inlet would have started and operated as designed, without major flow separation; this result is not consistent with the data. A qualitative study starting from the Mach 2.5 conditions showed the presence of massive separation at low-speed conditions. At reaching Mach 6.4 conditions, the inlet restarted but significant separation remained because of apparent hysteresis effects.

The separated flow in the inlet caused significant total pressure loss, lowering the combustor-entrance Mach number from an expected value of about 2.7 to an actual value near 2.0. With this lower Mach inlet condition, the resulting CFD solutions come close to the measured flight wall-pressure data. Both data and computations show the burner operating in a classical dual-mode, with large regions of subsonic reacting flow dominating the combustor. The present analysis indicates that the fuel was completely mixed, and that the combustion efficiency was 94% at the combustor exit.

Underlying assumptions meant to simplify calculations (i.e., steady-state analysis, uncoupled inlet and burner) may have been responsible for the numerical analysis not being able to quantitatively match the data and may have to be reconsidered. A complete-engine time-accurate calculation of the flight test from Mach 2.5 to 6.4 may be needed to accurately replicate inlet separation and combustor entrance conditions. In addition, turbulence and transport models for the highly-distorted combustor flow may need to be reassessed; the relaxation of the constant- Sc_T assumption should be a priority. As it stands, the present analysis showed that CFD is able to predict potential problems in a given design (and actual construction) so as to prevent them from occurring in an actual experiment or flight-test.

Acknowledgments

The author wishes to thank Randy Volland, Michael Smart and Aaron Auslender for their help in providing the experimental data, as well as their suggestions and comments. Rick Gaffney made available his unpublished report and gave useful advice. Robert Baurle assisted with one-dimensional processing of numerical results. Jeff White continued to provide support in the use of the VULCAN code for this and other projects. This research was initially funded by NASA grant NASW-4907 through the National Research Council, with Charles McClinton as technical advisor.

References

- ¹ McClinton, C., Roudakov, A., Semenov, V., and Kopehenov, V., "Comparative Flow Path Analysis and Design Assessment of an Axisymmetric Hydrogen Fueled Scramjet Flight Test Engine at a Mach Number of 6.5", AIAA Paper 96-4571, 1996.
- ² Volland, R.T., Auslender, A.H., Smart, M.K., Roudakov, A., Semenov, V., and Kopehenov, V., "CIAM/NASA Mach 6.5 Scramjet Flight and Ground Test", AIAA 99-4848, 1999.
- ³ Hawkins, R.W., "CFD Analysis of Oversped CIAM Scramjet at Mach 6.5", HNAG Report 96-1-071, NASA Langley Research Center, 1996.
- ⁴ Gaffney, R.L., and Sanetrik, M.D., "CFD Calculation of the CIAM SCRAMJET Engine Flowfield", unpublished report, 1999.
- ⁵ Rodriguez, C.G. "CFD Analysis of the CIAM/NASA Scramjet Engine (I): Inlet and Scramjet Analysis", HX Report HX-977, NASA Langley Research Center, 2001.
- ⁶ Rodriguez, C.G. "CFD Analysis of the CIAM/NASA Scramjet Engine (II): Inlet Unstart and Restart", HX Report HX-977, NASA Langley Research Center, 2001.
- ⁷ White, J.A., and Morrison, J.H., "A Pseudo-Temporal Multi-Grid Relaxation Scheme for Solving the Parabolized Navier-Stokes Equations", AIAA 99-3360, 1999.
- ⁸ Wilcox, D.C., *Turbulence Modeling for CFD*, 2nd. Edition, DCW Industries, Inc., 1998.
- ⁹ Drummond, J.P., Rogers, R.C., and Hussaini, M.Y., "A Detailed Numerical Model of a Supersonic Reacting Mixing Layer", AIAA 86-1427, 1986.
- ¹⁰ Rogers, R.C., "A Study of the Mixing of Hydrogen Injected Normal to a Supersonic Airstream", NASA TN D-6114, 1971.
- ¹¹ Eklund, D.R., Baurle, R.A., and Gruber, M.R., "Numerical Study of a Scramjet Combustor Fueled by an Aerodynamic Ramp Injector in Dual-Mode Combustion", AIAA Paper 2001-0379, 2001.

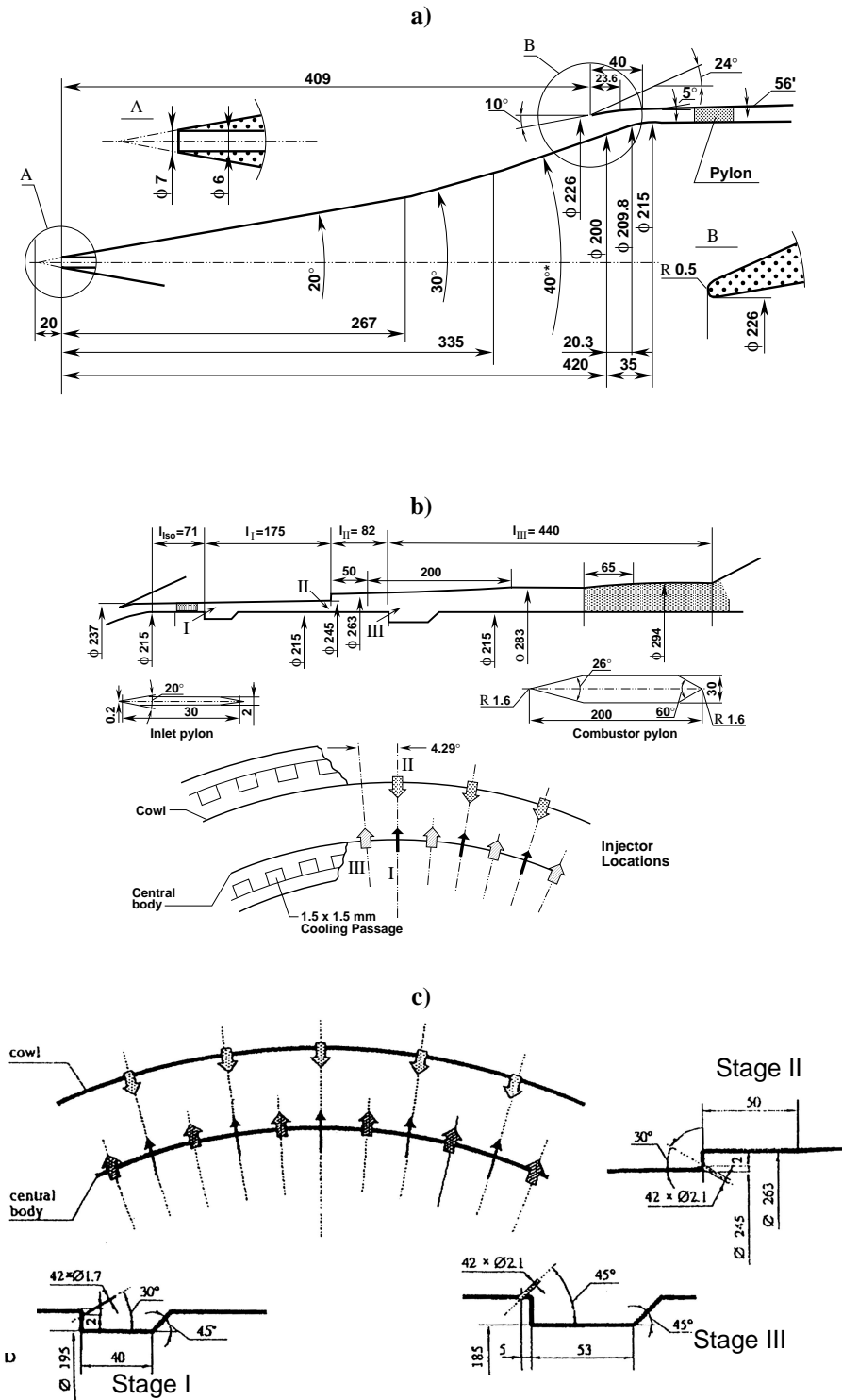


Figure 1: Inlet and combustor design geometry (units in mm; ϕ denotes diameter)
a) inlet; b) combustor; c) injector stages (courtesy R.T. Voland).

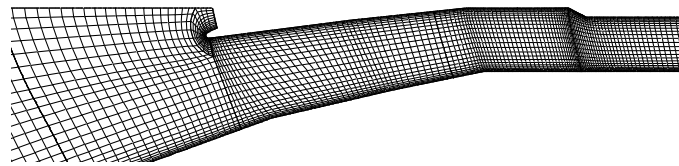
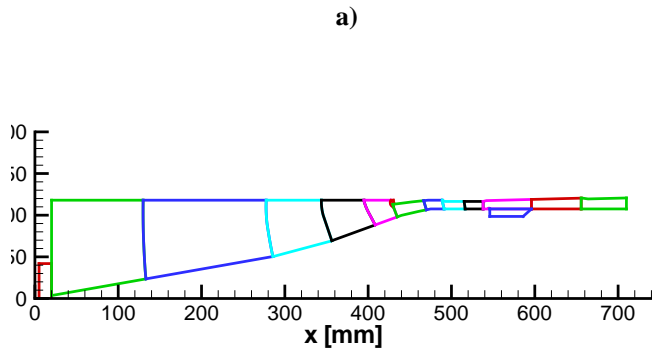


Figure 2: Inlet grid

a) Overall layout and block configuration - b) Close-up view near the throat (every 4th grid-line shown).

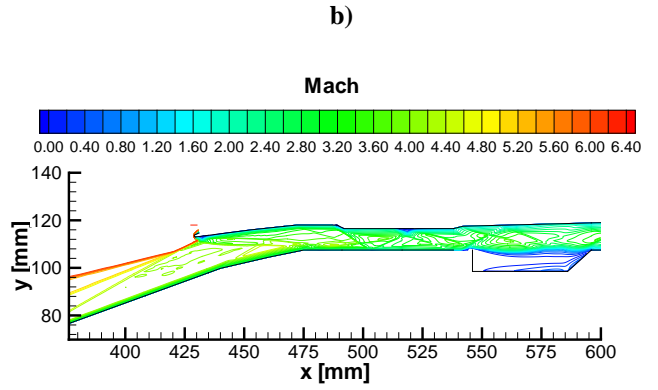
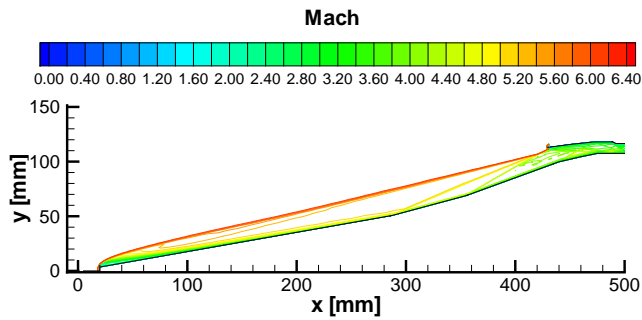


Figure 3: Inlet - Mach Contours

a) External Inlet - b) Internal inlet

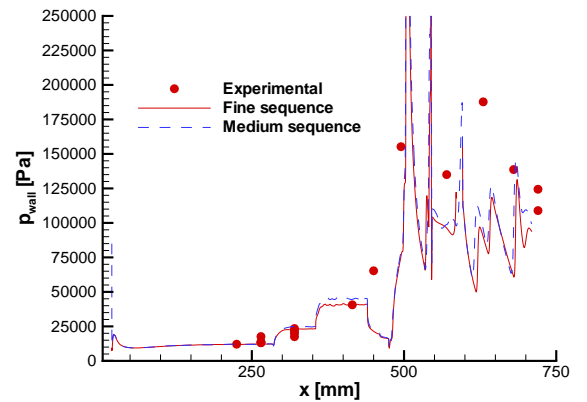
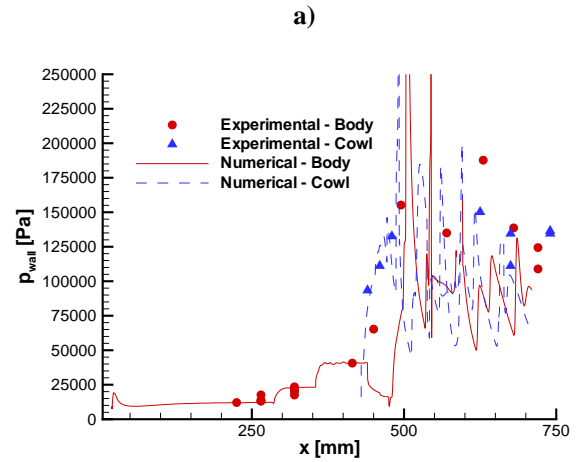


Figure 4: Inlet - Wall pressures

a) Body and cowl pressures - b) Grid convergence.

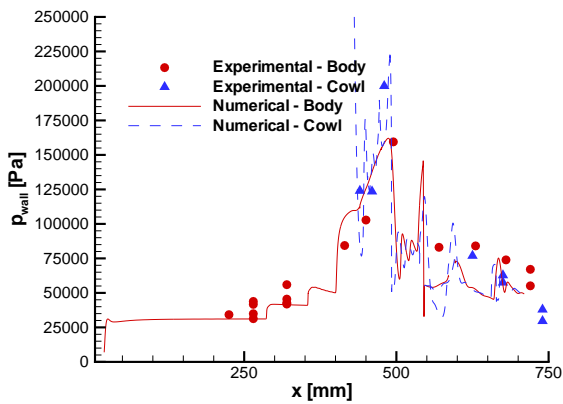
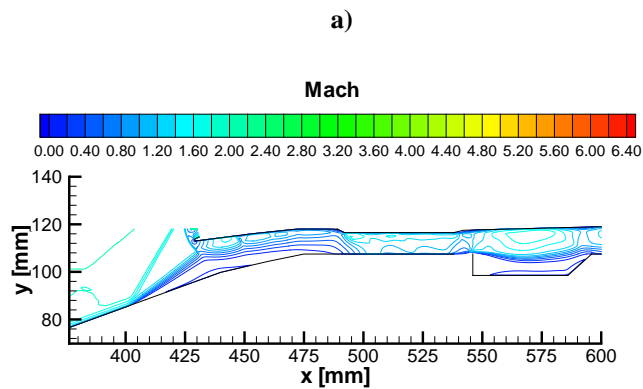


Figure 5: Inlet - $t = 25s$.
a) Mach contours - b) Wall pressures.

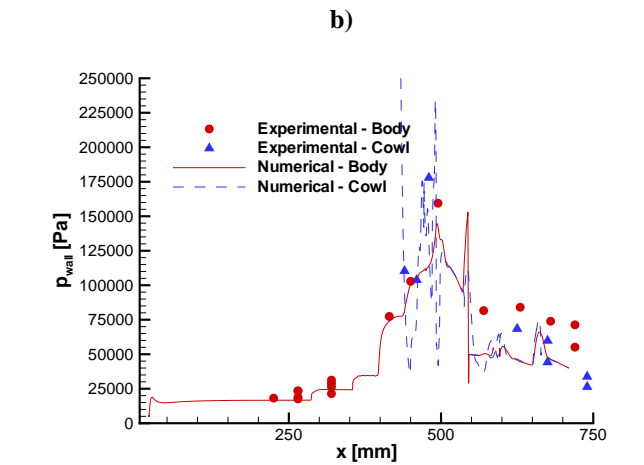
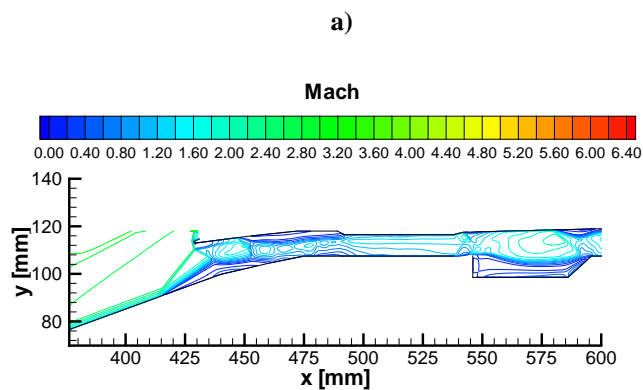


Figure 6: Inlet - $t = 38s$.
a) Mach contours - b) Wall pressures.

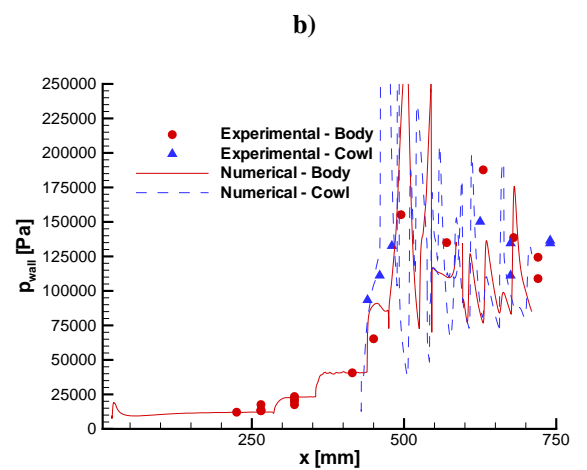
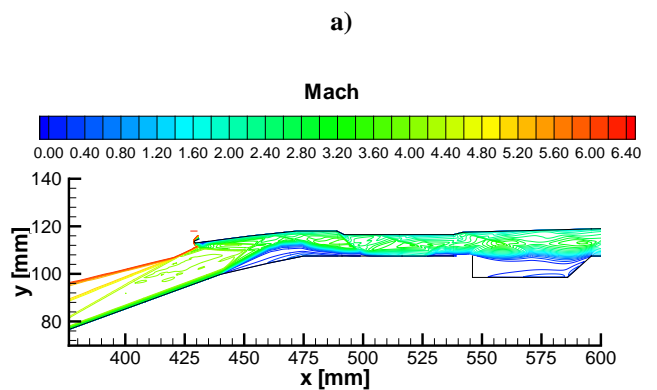


Figure 7: Inlet - $t = 56s$.
a) Mach contours - b) Wall pressures.

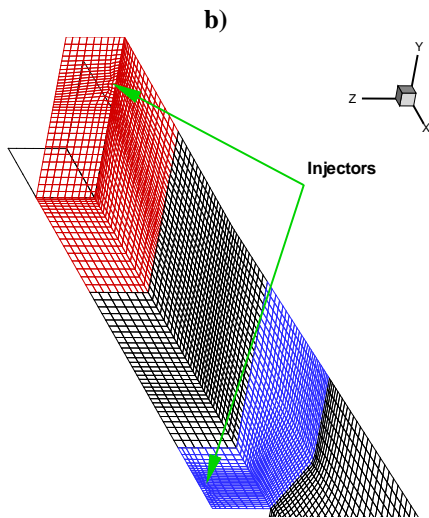
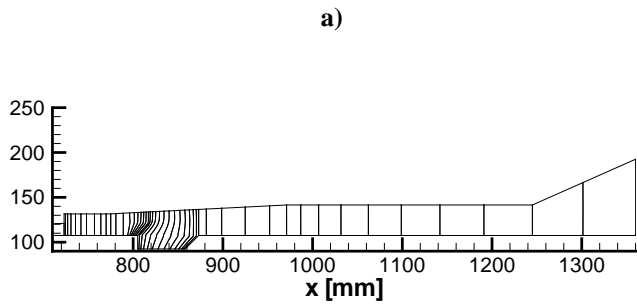


Figure 8: Burner grid

a) Overall layout and block configuration - b) Close-up view near the injectors (every 4th grid-line shown).

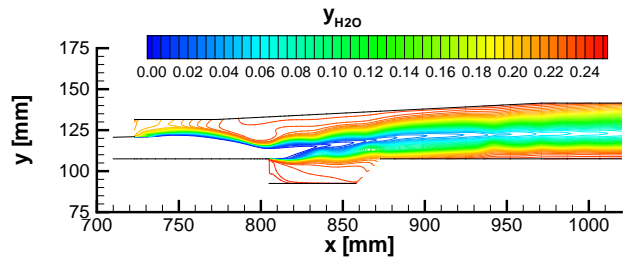


Figure 10: Burner - Water contours.

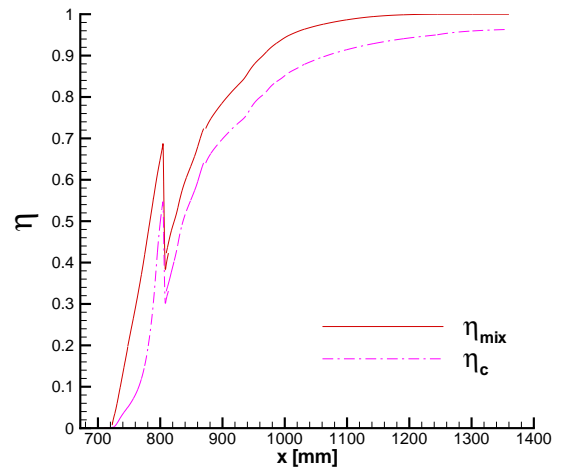


Figure 11: Burner - Mixing- and combustion-efficiency distributions.

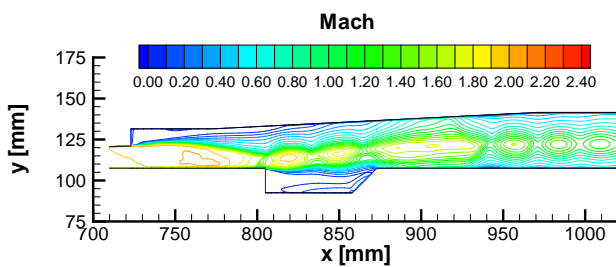


Figure 9: Burner - Mach contours.

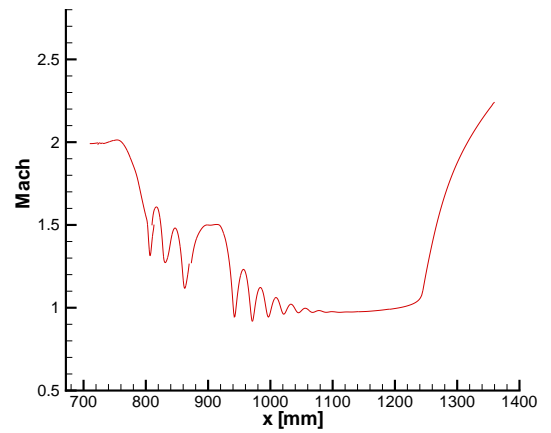


Figure 12: Burner - One-dimensional Mach distribution.

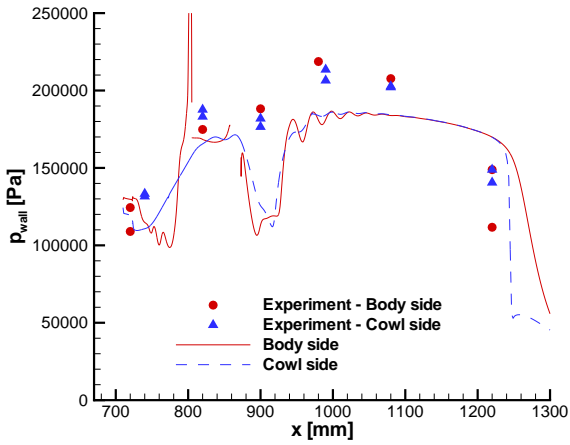


Figure 13: Burner - Wall pressures.

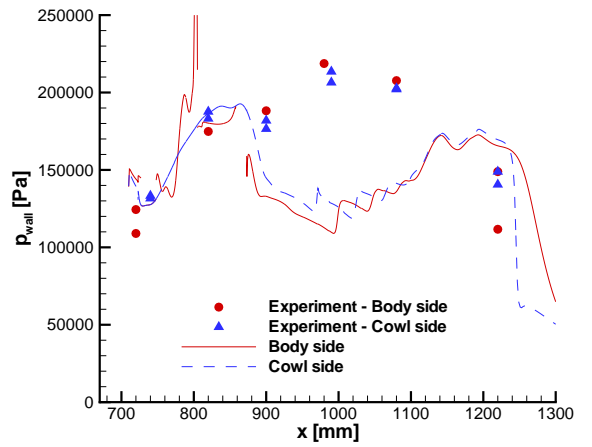


Figure 15: Burner - Cowl-wall pressure distributions for $Sc_T = 0.5$.

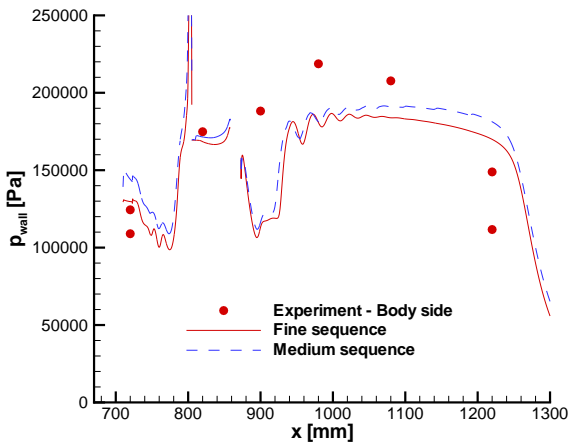


Figure 14: Burner - Cowl-wall pressure distributions for medium and fine grid-sequences.

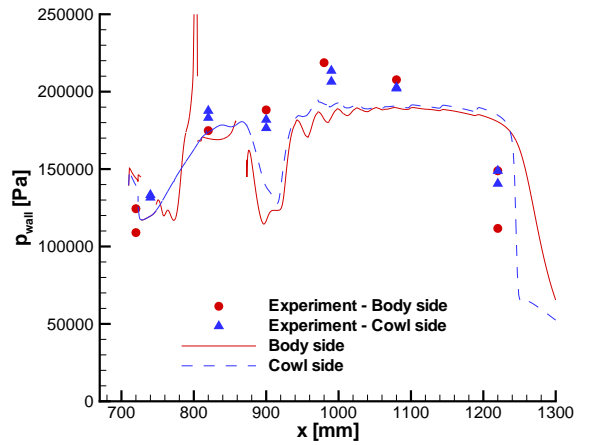


Figure 16: Burner - Cowl-wall pressure distributions for the 9 x 18 chemistry model.